

# Responses of polar energy budget to regional SST changes in extra-polar regions

Qingmin Wang<sup>1</sup>, Yincheng Liu<sup>1</sup>, Lujun Zhang<sup>1</sup>, Chen Zhou<sup>1,\*</sup>

<sup>1</sup>School of Atmospheric Science, Nanjing University, Nanjing, 210000, China

Correspondence to: Chen Zhou (czhou17@nju.edu.cn)

**Abstract.** Surface temperature at polar regions is not only affected by local forcings and feedbacks, but also depends on teleconnections between polar regions and low latitude regions. In this study, the responses of energy budget in polar regions to remote sea surface temperature (SST) changes are analysed using a set of idealized regional SST patch-perturbation experiments. The results show that responses of polar energy budget to remote sea surface warmings are regulated by changes in atmospheric energy transport, and radiative feedbacks also contribute to the polar energy budget at both the top-of-atmosphere (TOA) and surface. Specifically, An increase of poleward atmospheric energy transport to polar regions results in an increase of surface and air temperature, leading and the corresponding Planck feedback leads to a radiative warming at surface and radiative cooling at TOA. In response to sea surface warmings in most midlatitude regions, the poleward atmospheric energy transport to polar regions in the corresponding hemisphere increases. Sea surface warming over most tropical regions enhances the polar energy transport to both Arctic and Antarctic regions, except that an increase in the Indian Ocean's temperature results in a decrease in poleward atmospheric energy transport to the Arctic due to different responses of stationary waves. Sensitivity of Arctic energy budget to tropical SST changes is generally stronger than that of Antarctic energy budget, and poleward atmospheric heat transport is dominated by dry static energy, with a lesser contribution from latent heat transport. Polar energy budget is not sensitive to SST changes in most subtropical regions. These results help indicate that the explain how -effect of remote SST on the -polar climate climate -is affected by depends on the magnitude and spatial pattern of remote SST change.

## 1 Introduction

As global surface temperature increases, the Arctic region has experienced a surface temperature rise more than twice the global average (Lenssen et al., 2019), a phenomenon known as "Arctic Amplification" (AA). AA exemplifies the broader phenomenon of polar amplification. However, the mechanisms in the Antarctica region differ from the Arctic region due to factors like the high elevation of the Antarctic ice sheet, weaker albedo reduction and strong Southern Ocean heat uptake, which delay the response (Salzmann, 2017; Armour et al., 2016; Hahn et al., 2021; Smith et al., 2019), which is also applicable to the Antarctic. However, due to factors such as the higher average elevation of the Antarctic continent, its lower albedo, and

Formatted: Font color: Text 1

Formatted: Font color: Text 1

Formatted: Font color: Text 1

feedback efficiency differences, as well as the Southern Ocean's heat absorption capacity (Salzmann, 2017; Hahn et al., 2021), the warming in Antarctica appears more moderate compared to the Arctic (Marshall 2015; Smith, 2019).

The polar energy budget (PEB) is highly sensitive to various local feedback mechanisms. One important mechanism is the ice-albedo feedback. Global warming reduces snow coverClimate warming reduces polar region snow cover and sea ice cover in the polar regions, leading to more solar radiation being absorbed, which in turn accelerates climate warming and further decreases albedo (Dickinson et al., 1987; Hall, 2004; Boeke and Taylor, 2018; Duan et al., 2019; Dai et al., 2019). Additionally, temperature feedback is another significant contributor to AA (Pithan and Mauritsen, 2014; Láin   et al., 2016; Sejas and Cai, 2016). It involves the processes of radiative cooling and is characterized by the Planck and lapse-rate feedbacks. The Planck feedback, driven by the nonlinear relationship between blackbody radiation and temperature, provides negative feedback to TOA fluxes at all latitudes, especially in low latitudes (Pierrehumbert, 2010). The lapse-rate feedback is a significant driver of AA: in the Arctic regions, stable stratification and temperature inversions trap surface warming and reduce radiative cooling, thereby enhancing warming. In contrast, the tropics experience significant upper-atmosphere warming due to convection, which does not similarly trap heat (Pithan and Mauritsen, 2014). This feedback mechanism forms a positive feedback loop, making the warming in the Arctic more pronounced compared to other regions. Additionally, temperature feedback is another significant contributor to AA (Pithan and Mauritsen, 2014; Láin   et al., 2016; Sejas and Cai, 2016). Temperature feedback manifests as increased downwelling longwave radiation due to atmospheric warming, which in turn heats the surface and increases upwelling longwave radiation, creating a positive feedback loop that amplifies surface and atmospheric warming (Sejas and Cai 2016; Vargas et al., 2019). During climate warming, the transformation of ice clouds into water clouds increases cloud albedo, leading to negative feedback (Mitchell et al., 1989; Li and Le Treut, 1992). Simultaneously, the decrease in lower tropospheric stability increases Arctic cloud cover and optical thickness (Barton et al., 2012; Solomon et al., 2014; Taylor et al., 2015; Yu et al., 2019), contributing to Arctic autumn and winter warming (Boeke and Taylor, 2018). These local feedbacks are considered primary contributors to Arctic amplification (Pithan and Mauritsen, 2014; Goosse et al., 2018; Hahn et al., 2021; Dai et al., 2019). These local feedback mechanisms collectively enhance Arctic warming.

However, polar climate is also shaped affected by both local feedback processes and remote influences, whose interaction drives Arctic warming (Li et al., 2021). While some studies suggest that remote forcing plays a relatively minor role in Arctic amplification (Stuecker et al., 2018), other research highlights the significant impact of poleward heat and moisture transport from lower latitudes in enhancing Arctic warming, and AA exists even in the absence of local sea-ice feedbacks (Alexeev et al., 2005; Graversen and Burtu, 2016). Specifically, poleward atmospheric heat transport (AHT) and moisture transport are critical components that contribute substantially to the observed warming in the Arctic.

Under global warming, the AHT from low latitudes is more effective in reaching the polar regions compared to the equatorward transfer from high latitudes (Alexeev et al., 2005; Chung and R  is  nen, 2011; Park et al., 2018; Shaw and Tan, 2018; Semmler et al., 2020). However, polar climate is not only influenced by local feedback processes, but is also highly sensitive to remote effects (Li et al., 2021). Specifically, meridional atmosphere heat transport (AHT) plays a crucial role in polar temperatures (Budyko, 1969; Sellers, 1969; North, 1975), and the efficiency of heat transfer from low latitude regions to the poles

Formatted: Font color: Text 1

Formatted: Font color: Text 1

Formatted: Font color: Text 1

Formatted: Font color: Text 1

significantly surpasses that from high latitude regions to the equator under global warming (Alexeev et al., 2005; Chung and Räisänen, 2011; Park et al., 2018; Shaw and Tan, 2018; Stuecker et al., 2018; Semmler et al., 2020), and m. Multiple global climate model experiments have been conducted to measure the remote influence on Arctic warming. These experiments include adding additional energy terms directly to the surface energy balance (Alexeev et al., 2005; Chung and Räisänen, 2011; Yoshimori et al., 2017; Park et al., 2018), using latitude restricted increases in CO<sub>2</sub> (Chung and Räisänen, 2011; Shaw and Tan, 2018; Stuecker et al., 2018; Semmler et al., 2020), and specifying increases in sea surface temperature (SST) in low-latitude regions (Yoshimori et al., 2017). The transport of water vapor from mid-latitudes also plays an important role by enhancing the greenhouse effect prior to condensation and increasing cloudiness after condensation, which together warm the Arctic during winter (Graversen and Burtu, 2016). Graversen and Burtu (2016) showed that latent heat transport can lead to significantly more Arctic warming than dry static energy (DSE) transport, even when delivering an equivalent amount of energy. Therefore, remote processes play an important, significant role in driving Arctic warming, and the remote forcings are further amplified by local feedback processes. These studies indicate that a portion of Arctic warming is induced by indirect effects of remote warming. It is estimated that 50%–85% of Arctic warming is induced by non-local drivers (Chung and Räisänen, 2011; Yoshimori et al., 2017; Park et al., 2018; Shaw and Tan, 2018; Stuecker et al., 2018). Local Arctic feedbacks further amplify this remotely induced Arctic warming, resulting in the final remotely induced warming, accounting for half or more of the total Arctic warming.

In low-latitude regions, sea surface temperature (SST) variations markedly affect the PEB polar energy budget (Alexeev et al., 2005). It is widely accepted that planetary waves play a critical role in establishing teleconnections between tropical oceans and polar regions. These waves are pivotal in the transport of heat and moisture to the Arctic, consequently driving the increase in polar temperatures (Graversen and Burtu, 2016; Baggett and Lee, 2017). For instance, intensified convective activity within the Pacific Warm Pool not only strengthens the propagation of Rossby waves toward the poles but also increases the frequency of these fluctuations. This enhancement in Rossby wave activity boosts the transport of water vapor to the Arctic, augmenting the downward longwave radiation in the Arctic regions (Rodgers et al., 2003; Lee et al., 2011; Lee, 2012; Lee, 2014). While synoptic-scale transient eddies contribute significantly to mean-state poleward heat transport and its changes under increased CO<sub>2</sub> (Donohoe et al., 2020), their overall impact is relatively minor compared to that of amplified planetary waves in responses to tropical warming (Baggett and Lee, 2017). While synoptic-scale waves also contribute to the transport of heat and moisture to the Arctic, their overall impact is relatively minor and becomes significant mainly in the context of amplified planetary waves (Baggett and Lee, 2017). Atmospheric circulation models reveal that warming of tropical SST from glacial to interglacial periods significantly elevates summer temperatures in regions where the Canadian ice sheet forms. This high-latitude response arises from small amplitude extra-annular climate changes, which alter the vertical distribution of atmospheric temperature and water vapor in the extra-annular zone, primarily through atmospheric bridging mechanisms. Conversely, cold tropical SST variations/perturbations exert a lesser impact on water vapor transport and temperature in the Canadian region (Rodgers et al., 2003). The tropical SST anomalies during El Niño and La Niña events have large impact on Arctic surface air temperature (Lee et al., 2011; 2012; 2014), but the impacts of major El Niño events on Arctic temperatures

Formatted: Font color: Text 1

Formatted: Font color: Text 1

are distinct due to differences in eastern tropical Pacific SST (Jeong et al., 2022), indicating that the amplitude and spatial pattern of SST change is important for Arctic climate predictions. The "Tropical Excitation of Arctic Warming Mechanisms" (TEAM) further elucidates this phenomenon: increased polar moist static energy transport during La Niña episodes leads to Arctic winter surface warming, whereas the opposite is true during El Niño episodes (Lee et al., 2011; 2012; 2014). Analysis of El Niño and La Niña composite data shows that localized tropical convective heating intensifies polar temperature anomalies.

In previous researches, scholars primarily focused on the impact of SST over a large area of tropical oceans on the [PEB polar energy budget](#). However, studies have indicated significant variations in the effects of SST anomalies in different oceanic regions on the global climate system (Barsugli and Sardeshmukh, 2002; Fletcher et al., 2011) (Barsugli, 2002; Fletcher, 2014). In this study, we employ a set of idealized SST ~~patch patches~~ experiments to perform a systematic analysis on the response of the [PEB polar energy budget](#) to SST changes in various areas.

## 2 Data and Method

### 2.1 Individual patch experiments

The patch experiments were conducted using the Community Earth System Model version 1.2.1 integrated with the Community Atmospheric Model 5.3 (CESM1.2.1-CAM5.3, Neale et al. (2012)), operating at a spatial resolution of 1.9° latitude by 2.5° longitude. The experimental setup included a control experiment and two sets of patch experiments—one with warm patches and another with cold patches. The control experiment spanned 41 years, maintaining the sea surface temperature (SST), sea ice, and climatic forcings at the constant present-day levels observed in the (year 2000). The global ocean was segmented into 80 overlapping rectangular areas, comprehensively covering the global ice-free ocean surface, as depicted in Figure 1 of Zhou et al. (2020). In the warm patch experiments, a positive SST anomaly was introduced at the ocean surface within a designated patch, while the SST in other regions is same as the control setup. Conversely, the cold patch experiments involved introducing a negative SST anomaly at the ocean surface within the respective patches. The SST anomalies in each patch were designed according to the equation proposed by Barsugli and Sardeshmukh (2002), which effectively mitigates nonlinearity due to unrealistic SST gradients, ensuring a more realistic simulation of oceanic temperature variations,

$$\Delta SST_p(lat, lon) = A \cos^2\left(\frac{\pi}{2} \frac{lat-lat_p}{lat_w}\right) \left(\frac{\pi}{2} \frac{lon-lon_p}{lon_w}\right), \quad (1)$$

where  $|lat - lat_p| < lat_w$ ,  $|lon - lon_p| < lon_w$ . The terms  $lat_p$  and  $lon_p$  are the latitude and longitude of the center point for a specific patch, respectively;  $lat_w$  and  $lon_w$  are the meridional and zonal half-width of the patch, respectively, with their values set to  $lat_w = 10^\circ$  and  $lon_w = 40^\circ$  in these experiments; and  $A$  is the amplitude of the SST anomaly, [which is set to be +4 K and -4 K in this study.](#)

Formatted: Font color: Text 1

Formatted: Font color: Text 1

In this study, we analyzed the responses of polar TOA radiative fluxes ( $R_{TOA}$ ), polar surface radiation fluxes ( $R_{sfc}$ ), and radiation heat fluxes resulting from atmospheric heat transport meridional atmospheric advection to the polar regions ( $R_{AHT}R_{adv}$ ). The equations for calculating these parameters are listed as follows:

$$R_{TOA} = FSNT - FLNT, \quad (2)$$

$$130 \quad R_{sfc} = FSNS - FLNS - SH - LH, \quad (3)$$

$$R_{AHT}R_{adv} = R_{sfc} - R_{toa}, \quad (4)$$

where  $FSNT$  represents the net downward shortwave radiation at the TOA,  $FLNT$  denotes the net upward longwave radiation at the TOA,  $FSNS$  is the net downward shortwave radiation at the surface,  $FLNS$  represents the net upward longwave radiation at the surface, and  $SH$  and  $LH$  account for the sensible and latent heat fluxes, respectively. Additionally, both  $SH$  and  $LH$  are defined as positive upward.

## 2.2 EOF-SST experiments

To quantify the ~~PEBPOLAR ENERGY BUDGET~~ polar energy budget response to realistic SST anomaly patterns, we applied EOF analysis to historical SST data from 1980 to 2019, and identified the first eight EOF modes. We then conducted eight separate EOF-SST experiments, and the SST of each experiment was perturbed by a specific EOF mode relative to the control run. These experiments allow us to isolate and understand the impact of realistic SST anomaly patterns on the ~~PEB~~ polar energy budget.

## 2.3 Radiative Kernel Decomposition Methodology

This study employs the radiative kernel approach (Soden et al., 2008, Huang et al., 2017) to decompose both surface and TOA radiation into the radiative effects of various meteorological variables, measured in watts per square meter ( $Wm^{-2}$ ). The core calculation involves multiplying the radiative kernels with the monthly anomalies of the corresponding climate fields as follows:

$$\Delta R_{X_s} = K_{X_s} \cdot \Delta X_s, \quad (5)$$

Here,  $X$  denotes an arbitrary non-cloud climate variable,  $\Delta R_{X_s}$  represents the radiative effect at the surface or TOA associated with that variable,  $K_{X_s}$  is the corresponding radiative kernel, and  $\Delta X$  is the monthly anomaly of the climate variable, calculated as the deviation from the monthly climatological average. Positive values of  $\Delta R$  indicate an increase in net incoming radiation, which corresponds to a warming effect on the Earth. The radiative kernels used in this analysis are derived from the ERA-Interim climatological fields and have been validated to perform well with climate model surface outputs (Huang et al., 2017; Liu et al., 2024).

Cloud radiative effects are calculated following the methodology of Soden et al. (2008):

$$155 \quad \Delta R_{Cld_s} = \Delta CRF - \sum_X (K_{X_s} - K_s^0) \Delta X \quad (6)$$

Formatted: Font color: Text 1

Formatted: Font: Times New Roman

Formatted: Font color: Text 1

Formatted: Font color: Text 1

Formatted: Font color: Text 1

Formatted: Font color: Text 1

Formatted: Font color: Text 1

Formatted: Font color: Text 1

Formatted: Font color: Text 1

Formatted: Font color: Text 1

Formatted: Font color: Text 1

Formatted: Font color: Text 1

Formatted: Font color: Text 1

Formatted: Font color: Text 1

Formatted: Font color: Text 1

Formatted: Font color: Text 1

Formatted: Font color: Text 1

Formatted: Font color: Text 1

Formatted: Font color: Text 1

Formatted: Font color: Text 1

Formatted: Font color: Text 1

Formatted: Font color: Text 1

Formatted: Font color: Text 1

Formatted: Font color: Text 1

Formatted: Font color: Text 1

Formatted: Font color: Text 1

Formatted: Font color: Text 1

Formatted: Font color: Text 1

In this equation,  $\Delta R_{cld}$  denotes the cloud-induced radiative anomalies, and CRF (Cloud Radiative Forcing) is defined as the difference in surface net radiation fluxes between all-sky and clear-sky conditions. The superscript <sup>0</sup> means the clear-sky kernels.

Building upon this framework, the study further decomposes the TOA and surface radiative anomalies into specific feedback components to achieve a more detailed analysis of the factors influencing the Earth's radiation balance.  $\Delta R_{TOA}$  is partitioned into cloud-induced radiative anomalies ( $\Delta R_{TOA,cld}$ ), albedo-induced radiative anomalies ( $\Delta R_{TOA,alb}$ ), Planck feedback-induced radiative anomalies ( $\Delta R_{TOA,pbk}$ ), and lapse-rate feedback-induced radiative anomalies ( $\Delta R_{TOA,LR}$ ). Similarly,  $\Delta R_{sfc}$  is broken down into cloud-induced surface radiative anomalies ( $\Delta R_{sfc,cld}$ ), albedo-related surface radiative anomalies ( $\Delta R_{sfc,alb}$ ), Planck feedback-induced surface radiative anomalies ( $\Delta R_{sfc,pbk}$ ), lapse-rate feedback-induced surface radiative anomalies ( $\Delta R_{sfc,LR}$ ), LH anomalies ( $\Delta R_{LH}$ )-induced radiative anomalies ( $\Delta R_{LH}$ ), and SH anomalies ( $\Delta R_{SH}$ )-induced radiative anomalies ( $\Delta R_{SH}$ ).

### 3 Result

#### 3.1 Responses of PEB Polar Energy Budget to Local SST Changes

The differences of annual PEB polar energy budget in conjugate SST patch warming experiments and SST cooling experiments are shown in Figure 1. The location of each point denotes the center of corresponding patch, and the colors of these points denote the differences of PEB polar energy budget between corresponding conjugate warming and cooling patch experiments. Additionally, t-tests were conducted to assess their statistical significance. The difference between TOA radiation (Figure 1a, d) and surface radiation (Figure 1b, e) reflects atmospheric heat transport (Figure 1c, f).

Figures 1(a-c) show the responses of the Arctic energy budgets to SST warmings in global oceanic regions. In response to western and central tropical Pacific SST warming, there is a significant increase in poleward energy transport towards the Arctic regions (Figure 1c), as indicated by the positive poleward  $\Delta R_{AHT}$  near 60°N heat transport to the Arctic region (positive  $\Delta R_{AHT}$ ). This enhanced energy transport warms the Arctic atmosphere, leading to an increase in surface radiation (positive  $\Delta R_{sfc}$ ; Figure 1b) due to higher surface and air temperatures. Simultaneously, the warmer atmosphere emits more longwave radiation to space, resulting in a decrease in TOA radiation (negative  $\Delta R_{TOA}$ ; Figure 1a). Conversely, warming in the tropical Indian Ocean reduces the poleward energy transport to the Arctic region (negative  $\Delta R_{AHT}$ ), leading to cooler Arctic atmospheric temperatures, and there is a decrease in surface radiation (negative  $\Delta R_{sfc}$ ; Figure 1b) and increase in TOA radiation (positive  $\Delta R_{TOA}$ ; Figure 1a). Sea surface warming in the midlatitudes of the northern hemisphere increases Arctic surface radiation, but has insignificant impact on TOA radiation.

For the Antarctic energy budget, warming in the tropical Pacific and Indian Oceans generally leads to increased poleward energy transport (positive  $\Delta R_{AHT}$ ; Figure 1f), which warms the Antarctic atmosphere and results in increased Antarctic surface radiation (positive  $\Delta R_{sfc}$ ; Figure 1e) and decreased Antarctic TOA radiation (negative  $\Delta R_{TOA}$ ; Figure 1d). However, the

Formatted

Formatted

Formatted

Formatted

Formatted

Formatted

Formatted

Formatted

Formatted

Formatted

Formatted: Font: Not Bold

Formatted: Font: Not Bold

Formatted: Font color: Text 1, English (United Kingdom)

Formatted: Font color: Text 1

Formatted: Font color: Text 1

Formatted

Formatted

Formatted: Font color: Text 1

Formatted

Formatted

Formatted: Font color: Text 1

Formatted

Formatted

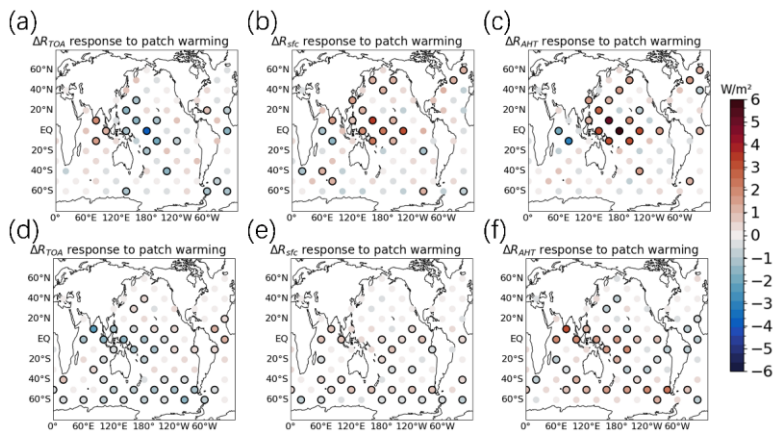
response of  $\Delta R_{TOA}$  to warmings in the tropical Atlantic is positive (Figure 1d). Warmings in the Southern Ocean also leads to an increase of Antarctic surface radiation and decrease in Antarctic TOA radiation. Antarctic energy budget is generally not sensitive to warmings in subtropical regions. Both  $\Delta R_{TOA}$  and  $\Delta R_{sfc}$  decrease in response to warmings in patches centred at 60°S, because patches centred at 60°S cover part of the Antarctic region (60°S to 90°S in this study), and the surface emit more energy to space as the sea surface warms, leading to a cooling radiative effect. Figure 1(a) shows the response of Arctic TOA radiation ( $R_{TOA}$ ) to global ocean warming. Significant changes are noted primarily in patches located in the tropical Indian Ocean and the eastern tropical Pacific. The response of Arctic  $\Delta R_{TOA}$  to SST warmings in the eastern tropical Pacific is negative, whereas the Arctic  $\Delta R_{TOA}$  response to warmings in the tropical Indian Ocean is positive. Additionally, there are several patches in the tropical Atlantic and near Antarctica contribute a negative Arctic  $R_{toa}$  anomaly. Figure 1(b) depicts the Arctic surface radiation response ( $R_{sfc}$ ) to global ocean warming. Significant changes can be found in patches located in the tropical Pacific and the tropical Indian Ocean. The response of  $R_{sfc}$  to warming in the tropical Pacific and the northwestern tropical Indian Ocean is positive, while the response to warming in the southeastern tropical Indian Ocean is negative. Figure 1(c) shows the response of meridional atmospheric advection near 60°N ( $R_{adv}$ ) to global ocean warming. Similar to the  $R_{sfc}$  response, significant responses can be found in patches located in the tropical Pacific and the tropical Indian Ocean. The response of  $R_{adv}$  to warming in the tropical Pacific and the northwestern tropical Indian Ocean is positive, while the response to warming in the southeastern tropical Indian Ocean is negative.

Figure 1(d-f) illustrates the Antarctic  $R_{TOA}$ ,  $R_{sfc}$  and  $R_{adv}$  response to global ocean warming. The response of  $\Delta R_{toa}$  to warming in the tropical Indian Ocean, tropical Pacific Ocean, and Southern Ocean is negative, while the response to warming in the tropical Atlantic is positive. The response of  $\Delta R_{sfc}$  to warmings in most tropical regions and part of the Southern Ocean is positive, while the response of  $\Delta R_{sfc}$  to warmings around 60°S is negative. The response of  $\Delta R_{adv}$  to warmings in the tropical Indian Ocean, tropical Pacific Ocean, and part of the Southern Ocean is positive.

The response of Arctic  $\Delta R_{AHT}$  to tropical warmings is generally greater than Antarctic  $\Delta R_{AHT}$ , indicating that more heat is transported to the Arctic region than that to the Antarctic region when the tropics warms. This difference may partly contribute to the faster Arctic warming than Antarctic warming under global warming. Surface characteristics and feedback mechanisms also differ markedly: the Antarctic's thick ice sheet, high altitude, and consistently high albedo leads to a weak ice albedo feedback (Budyko, 1969), whereas the Arctic's temperature sensitive sea ice produces a strong positive feedback as ice melt exposes low albedo seawater, enhancing solar radiation absorption (Pithan & Mauritsen, 2014).

- Formatted: Font color: Text 1
- Formatted: Font color: Text 1
- Formatted: Font color: Text 1
- Formatted: Font color: Text 1
- Formatted: Font color: Text 1
- Formatted: Font color: Text 1
- Formatted: Font color: Text 1
- Formatted: Font color: Text 1
- Formatted: Font color: Text 1
- Formatted: Font color: Text 1
- Formatted: Font: (Default) +Body (Times New Roman), Font color: Text 1

Formatted: Font: (Default) +Body (Times New Roman), Font color: Text 1, English (United States)



**Figure 1: Responses of polar energy budget to regional SST changes.** (a) Differences of Arctic (60°N-90°N) annual mean net TOA radiative fluxes ( $\Delta R_{TOA}$ ) between conjugate warming and cooling patch experiments. (b) Differences of Arctic annual mean net surface radiative fluxes ( $\Delta R_{sfc}$ ). (c) Differences of heat fluxes due to atmospheric heat transport to the Arctic regions ( $\Delta R_{AHT}$ ). (d-e) Responses of  $\Delta R_{TOA}$ ,  $\Delta R_{sfc}$ , and  $\Delta R_{AHT}$  in the Antarctic regions. The location of each point denotes the center of corresponding patch, and the colors denotes the differences between conjugate warming and cooling patch experiments. Black circles denote that the differences are statistically significant at 95% confidence level.

The responses of [PEBpolar energy transportbudget](#) depend on the season. The spatial distribution of the Arctic [PEBpolar energy budget](#) (Figure 2a-e) response to regional SST in boreal winter (DJF) (Figure 2a-c) is similar to the annual average values (Figure 1a-c), but the magnitude of DJF responses is greater than annual responses. For the Antarctic regions, the response of DJF [PEBpolar energy budget](#) to tropical ocean warming aligns with the annual average values.



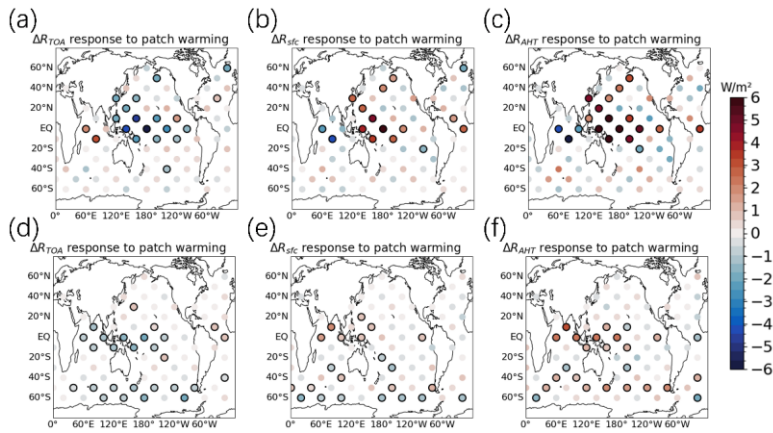


**Figure 2:** Similar to Same as Figure 1, but for the DJF season.

During boreal summer (JJA), the spatial distribution of Arctic ~~PEB~~~~POLAR ENERGY BUDGET~~~~polar energy budget~~ responses (Figures 3a-c) differ from the annual average. Specifically, the responses of  $\Delta R_{AHT}$   $\Delta R_{adv}$  to warmings in both the eastern Indian Ocean and western Pacific Ocean are positive. The responses of  $\Delta R_{sfc}$  and  $\Delta R_{TOA}$  in most patch experiments are statistically insignificant. Conversely, the Antarctic ~~PEB~~~~POLAR ENERGY BUDGET~~~~polar energy budget~~ responses to tropical ocean warming in JJA are similar to annual mean values.

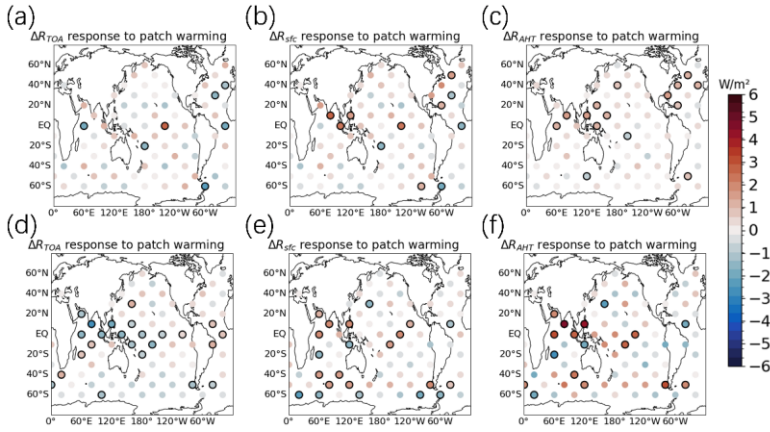


Figure 3: Same as Figure 1, but for the JJA season.

### 3.2 Comprehensive Reconstruction of Polar Energy Budgets Using Green's Function and Radiative Kernel Approaches

The response of polar energy budget to regional SST changes might be used to qualitatively explain how SST variations affect polar energy budget.

The sensitivity of the polar energy budget to SST perturbations within a specific grid box, identified by index  $i$ , can be estimated using the following equation (Zhou et al. 2017):

$$\left( \frac{\partial R}{\partial SST_i} \right)_p = \frac{\sum_p \Delta SST_p \left( \frac{\partial R}{\partial SST_i} \right)_p}{\sum_p \Delta SST_p} = \frac{\sum_p \Delta SST_p \frac{\partial R}{\partial SST_p} \frac{\partial R}{\partial SST_p} \frac{\partial R}{\partial SST_p} \frac{\partial R}{\partial SST_p}}{\sum_p \Delta SST_p} \quad (7)$$

where  $R$  denotes a specific energy flux,  $SST_i$  denotes the SST in the  $i$ -th grid box,  $S_i$  and  $S_p$  represent the ocean surface area of the specific grid point and the patch, respectively, and  $\Delta SST_p$  is the SST anomaly of the  $i$ -th grid in the  $p$ -th patch [Eq. (1), noting that  $\Delta SST_p$  equals zero for grid-points outside of a patch], and  $SST_i$  denotes the SST in the  $i$ -th grid box.  $\left( \frac{\partial R}{\partial SST_i} \right)_p$  reflects the average response of  $R$  to a 1-K increase in SST within a specific grid box inside the patch. Additionally,  $\frac{\partial R}{\partial SST_p}$  illustrates the variation in the polar energy budgetsensitivity of  $R$  to per unit of patch-averaged SST change, which is derived from experiments involvingfor the corresponding conjugate  $\pm 1$ -K patch warming and cooling experiments. The

Formatted: Font: Italic

sensitivity for grid boxes within a single patch corresponds to the average  $R$  change due to a 1 K warming within that specific grid box. For grid boxes overlapping multiple patches, the sensitivity is determined by the weighted average value  $\left(\frac{\partial R}{\partial SST_i}\right)_p$ . The sensitivities of polar energy budget to SST perturbation in each grid box are shown in Figure 4.

Utilizing these sensitivities, we can reconstruct the polar energy budget response to arbitrary changes in SST through the Green's function approach, represented as:

$$\Delta R = \sum_i \frac{\partial R}{\partial SST_i} \Delta SST_i + \varepsilon_i, \quad (8)$$

where  $\varepsilon_i$  is an error term, which represents the contributions from nonlinearities and non-SST induced factors.

Then we use the Green's function approach to reconstruct the  $\Delta R_{AHT}$  in response to 8 different SST patterns in the EOF-SST experiments (Figures. 5a-h), and the Green's function reconstructed  $\Delta R_{AHT}$  are then compared to model-produced values in the EOF-SST experiments (Figures. 5i-j). The results show that the majority of the experimental simulations of  $\Delta R_{AHT}$  align closely with the  $\Delta R_{AHT}$  reconstructed by the Green's function, lying near the  $y = x$  line. The biases of the Green's function reconstructed values are partially induced by the SST change inside the Arctic region, which is not captured by the Green's function reconstruction, and non-linear terms also contribute to the bias. Therefore, the Green's function approach can qualitatively explain how the SST perturbation patterns in Figure 5(a-h) affects polar energy budget.

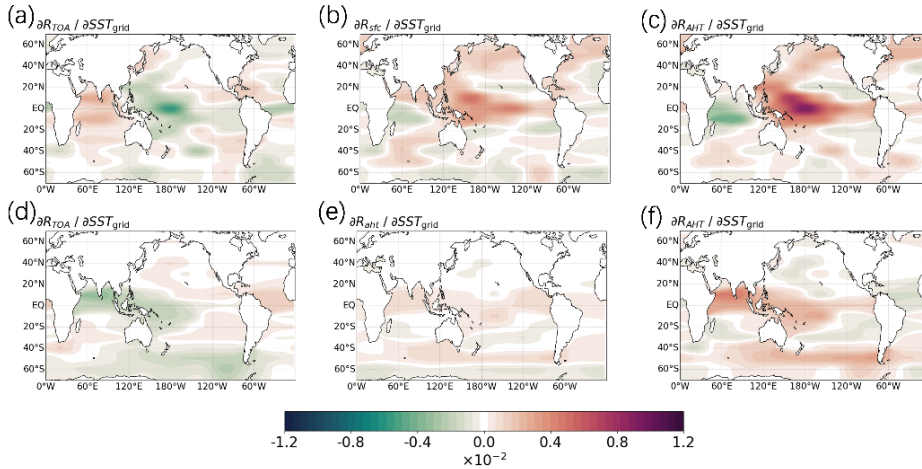


**Figure 4: The sensitivity of (a)  $\partial R_{TOA}/\partial SST_i$  of Arctic, (b)  $\partial R_{sfc}/\partial SST_i$  of Arctic, (c)  $\partial R_{AHT}/\partial SST_i$  of Arctic, (d)  $\partial R_{TOA}/\partial SST_i$  of Arctic, (e)  $\partial R_{sfc}/\partial SST_i$  of Arctic, (f)  $\partial R_{AHT}/\partial SST_i$  of Antarctica to surface warming in each grid box, calculated using Eq. (7). The units are  $W/m^2/K$ .**

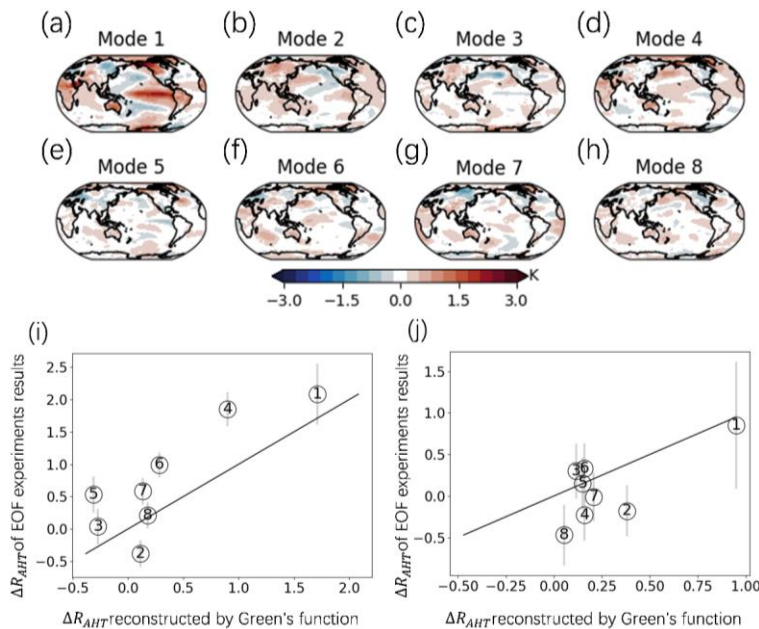


Figure 5: (a-h) The surface temperature change patterns in individual EOF-SST experiments. (i) Comparison of Arctic  $\Delta R_{AHT}$  responses to different SST change patterns in EOF-SST experiments (y-axis) and that reconstructed by the Green's function approach (x-axis). All values are averaged annually in this figure. The digits represent the number of corresponding EOF modes in each experiment. Error bars correspond to the 95 % confidence interval. (j) Response of Antarctica  $\Delta R_{AHT}$ .

### 3.3 Decomposition of polar energy budget responses with radiative kernels

To understand the mechanism how **PEB** polar energy budget is affected by remote SST, we quantify the contributions of meteorological factors to **PEB** polar energy budget responses (Figures- 64-75) using radiative kernels (Huang et al., 2017).

Figure 4a-6a shows that the contribution of cloud changes is relatively small to the Arctic  $\Delta R_{TOA}$  response. Nonetheless,

Pacific SST warming results in a negative Arctic  $\Delta R_{TOA, cld}$ , whereas Indian Ocean warming generates a positive Arctic  $\Delta R_{TOA, cld}$ . Albedo exhibits a positive response in both the tropical Indian Ocean and the Pacific Ocean (Figure 6a). The impact of Arctic  $\Delta R_{TOA, plk}$  exhibits a positive response to SST increases in the tropical Indian Ocean and a negative response

Formatted: Font: Not Bold, English (United Kingdom)

Formatted: Heading 2

Formatted: Font: (Default) Times New Roman

Formatted: Font color: Text 1

Formatted: Font color: Text 1

Formatted: Font color: Text 1

Formatted: Font color: Text 1

Formatted: Font color: Text 1

Formatted: Font color: Text 1

Formatted: Font color: Text 1

Formatted: Font color: Text 1

Formatted: Font color: Text 1

Formatted: Font color: Text 1



**Figure 6: Difference of annual mean  $\Delta R_{TOA,clt}$  (a),  $\Delta R_{TOA,alb}$  (b),  $\Delta R_{TOA,plk}$  (c),  $\Delta R_{TOA,LR}$  (d) for Arctic and annual mean  $\Delta R_{TOA,clt}$  (e),  $\Delta R_{TOA,alb}$  (f),  $\Delta R_{TOA,plk}$  (g),  $\Delta R_{TOA,LR}$  (h) for Antarctica between conjugate warming and cooling patch experiments.**

**Figure 4: Difference of annual mean  $\Delta R_{TOA,clt}$  (a),  $\Delta R_{TOA,alb}$  (b),  $\Delta R_{TOA,plk}$  (c),  $\Delta R_{TOA,LR}$  (d) for Arctic and annual mean  $\Delta R_{TOA,clt}$  (e),  $\Delta R_{TOA,alb}$  (f),  $\Delta R_{TOA,plk}$  (g),  $\Delta R_{TOA,LR}$  (h) for Antarctica between conjugate warming and cooling patch experiments.**

Figure 5-7 shows the contributions of meteorological factors to the responses of Arctic and Antarctic  $\Delta R_{sf_c}$ . For the Arctic, the spatial distribution of clouds' contribution to Arctic  $\Delta R_{sf_c}$  is similar to that for Arctic  $\Delta R_{TOA}$ , but the values are significantly higher (Figure 7b). The response of Arctic  $\Delta R_{sf_c,alb}$  closely resembles that of  $\Delta R_{TOA,alb}$ , with similar magnitudes (Figure 7a). Similar to the response of Arctic  $\Delta R_{TOA,plk}$ , the Arctic  $\Delta R_{sf_c,plk}$  response is also strong (Figure 7c), but the signs of  $\Delta R_{sf_c,plk}$  responses are generally opposite to those of  $\Delta R_{TOA,plk}$  response. Similar to the Planck feedback, the response of Arctic  $\Delta R_{sf_c,LR}$  to tropical ocean warming also shows signs opposite to those of  $\Delta R_{TOA,LR}$  (Figure 7d). Over the tropical Indian Ocean, Planck feedback is positive in the northern region and negative in the southern region, whereas lapse-rate feedback is consistently negative across the entire tropical Indian Ocean. Overall, Planck feedback remains dominant for the Arctic  $\Delta R_{sf_c}$ . The responses of Arctic  $\Delta LH$  and  $\Delta SH$  are negative in response to warmings in the tropical western Pacific and positive in response to warmings in the tropical Indian Ocean (Figure 7e, f). However, the response of Arctic  $\Delta R_{LH}$  and Arctic  $\Delta R_{SH}$  are relatively small, suggesting that, though these factors have a limited minor impact on Arctic  $\Delta R_{sf_c}$ . The negative responses of Arctic  $\Delta LH$  and  $\Delta SH$  in response to warmings in the tropical western Pacific indicate a suppression of upward turbulent heat fluxes at the Arctic surface, primarily due to enhanced energy transport from lower latitudes into the Arctic region. As warm air masses are advected poleward, the associated increase in downward longwave radiation warms the Arctic surface. This warming stabilizes the lower atmospheric boundary layer, thereby reducing the vertical turbulence necessary for effective heat exchange between the surface and the atmosphere. Similar to the Arctic regions, the contribution of cloud to Antarctic  $\Delta R_{sf_c}$  is negligible (Figure 7h). Albedo has no significant impact on Antarctic  $\Delta R_{sf_c}$  (Figure 7g), because sea ice concentration is fixed in these patch experiments and snow cover in Antarctica does not change significantly in these experiments. The Planck feedback dominates the contributions to Antarctic  $\Delta R_{sf_c}$ , with Antarctic  $\Delta R_{sf_c,plk}$  responding positively to tropical ocean warming (Figure 7i). Similar to the Arctic, the lapse-rate feedback contributes less significantly to  $\Delta R_{sf_c}$  (Figure 7j). Antarctic  $\Delta LH$  and  $\Delta SH$  show minimal responses with opposite signs to  $\Delta R_{sf_c,plk}$  (Figures 7k, l). For the Arctic, clouds have negligible contribution to Arctic  $\Delta R_{sf_c}$  (Figure 5a). The response of Arctic  $\Delta R_{sf_c,alb}$  is similar as that of  $\Delta R_{TOA,alb}$  (Figure 5b). Similar to the response of Arctic  $\Delta R_{TOA,plk}$ , the Arctic  $\Delta R_{sf_c,plk}$  response is also strong (Figure 5c), but the signs of  $\Delta R_{sf_c,plk}$  responses are generally opposite from those of  $\Delta R_{TOA,plk}$  response. Notably, the response of Arctic  $\Delta R_{sf_c,LR}$  to tropical ocean warming is significantly greater than that of  $\Delta R_{TOA,LR}$ . The sign of Arctic  $\Delta R_{sf_c,LR}$  is opposite to that of Arctic  $\Delta R_{TOA,LR}$ , but they exhibit similar spatial distributions (Figure 5d). This indicates that an increase in  $T_a$  leads to radiative warming to the surface, but the surface loses

Formatted: Font: Not Bold

Formatted: Font: Not Bold

Formatted: Font: Not Bold

Formatted: Font: Not Bold

Formatted: Font: Not Bold

Formatted: Font: Not Bold

more energy by emitting more thermal radiation after the surface is warmed up. The responses of Arctic  $\Delta R_{sfc,TH}$  and Arctic  $\Delta R_{sfc,SH}$  are negative in response to warmings in the tropical Pacific and positive in response to warmings in the tropical Indian Ocean (Figure 5e, f); however, these responses are relatively small, suggesting that these factors have a limited impact on Arctic  $\Delta R_{sfc}$ .

Similar to the Arctic regions, the contribution of cloud to Antarctic  $\Delta R_{sfc}$  is also negligible (Figure 5g). Albedo has no significant impact on Antarctic  $\Delta R_{sfc}$  (Figure 5h), because sea ice concentration is fixed in these patch experiments and snow cover in the Antarctica does not change significantly in these experiments.  $T_a$  and  $T_s$  are the main contributors to Antarctic  $\Delta R_{sfc}$ , with Antarctic  $\Delta R_{sfc,Ta}$  responding positively and Antarctic  $\Delta R_{sfc,Ts}$  responding negatively to tropical ocean warming (Figure 5i, j). The responses of Antarctic  $\Delta R_{sfc,LH}$  and  $\Delta R_{sfc,SH}$  are minimal (Figure 5k, l). These results suggest that while temperature adjustments are notable in Antarctica, responses of cloud cover and surface heat fluxes to remote SST warming have a small impact on Antarctic  $\Delta R_{sfc}$ .



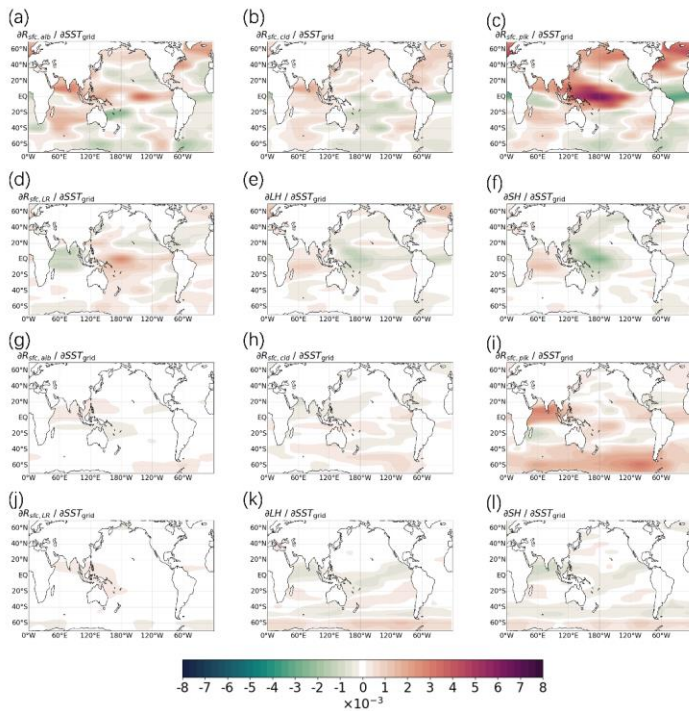


Figure 7: Difference of annual mean  $\Delta R_{sfc,clt}$  (a),  $\Delta R_{sfc,alb}$  (b),  $\Delta R_{sfc,plk}$  (c),  $\Delta R_{sfc,LR}$  (g),  $-\Delta LH$  (h),  $-\Delta R_{LH}$  (b),  $\Delta SH$  (i),  $\Delta R_{SH}$  (i) for the Arctic region, and annual mean  $\Delta R_{sfc,clt}$  (d),  $\Delta R_{sfc,alb}$  (e),  $\Delta R_{sfc,plk}$  (f),  $\Delta R_{sfc,LR}$  (j),  $\Delta LH$  (k),  $-\Delta R_{LH}$  (k),  $\Delta SH$  (l),  $\Delta R_{SH}$  (l) for the Antarctic region between conjugate warming and cooling patch experiments.

The Arctic exhibits larger contributions from clouds, albedo, LH and SH to  $\Delta R_{TOA}$  and  $\Delta R_{sfc}$  compared to Antarctica, which may partly explain the faster Arctic warming. Differences in cloud feedbacks play a significant role: the dry and cold Antarctic atmosphere limits cloud formation, resulting in a smaller impact on radiation fluxes (Lubin et al., 2006), while the Arctic's increased moisture transport from lower latitudes enhances cloud formation, significantly affecting surface and TOA radiation (Vavrus et al., 2004). Surface characteristics and feedback mechanisms also differ markedly: the Antarctic's thick ice sheet

Formatted: Font: Italic

Formatted: Font: Italic

Formatted: Font: Italic

Formatted: Font: Italic

Formatted: Font color: Text 1



high altitude, and consistently high albedo leads to a weak ice albedo feedback (Budyko, 1969), whereas the Arctic's temperature-sensitive sea ice produces a strong positive feedback as ice melt exposes low-albedo seawater, enhancing solar radiation absorption (Pithan & Mauritsen, 2014).

### 3.2.43 AHT responses to Regional SST Changes

According to Figures (46-57), the Planck feedback, which is primarily driven by changes in temperature, air temperature change is the primary contributor to PEB polar energy budget responses in these experiments. The sign of  $\Delta R_{AHT}$   $\Delta R_{adv}$  is generally same as  $\Delta R_{sfc,plk}$   $\Delta R_{sfc,toa}$ , and opposite from  $\Delta R_{TOA,T_{aplk}}$ . In addition, the difference between TOA and surface energy budget reflects the contribution of changes in polar AHT. Therefore, AHT plays a critical role in determining PEBPOLAR-ENERGY-BUDGET polar energy budget by changing the air temperature of polar regions. The responses of AHT to SST perturbations in the midlatitudes are consistent with our intuition, but the opposite Arctic AHT responses to SST warming over the tropical Indian Ocean and tropical Pacific Ocean requires further investigations.

To explore the underlying mechanisms of this phenomenon, we compared the climate responses to warmings in two illustrative patches within the tropical Pacific Ocean (TPO) and Indian Ocean (TIO). The center of the illustrative TPO patch is (180°E, 0°N), and the center of the illustrative TIO is (60°E, 0°N).

Figure 8 presents the responses of surface temperature ( $\Delta T_s$ ), 200hPa geopotential height ( $\Delta Z_{200}$ ), and 500hPa geopotential height ( $\Delta Z_{500}$ ) to warmings in these patches, providing background information to later AHT studies. Consistent with previous studies (Annamalai et al., 2007; Barsugli & Sardeshmukh, 2002; Ding et al., 2014), our experiments reveal that SST anomalies in different ocean basins induce contrasting atmospheric circulation patterns, primarily through Rossby wave responses affecting the Pacific-North American (PNA) pattern.

Specifically, warming in the TPO region leads to  $\Delta T_s$  increase over the Tibetan Plateau, Eastern Europe, tropical Africa, northeastern North America, and most of Antarctica. Concurrently,  $\Delta Z_{200}$  exhibits a local increase over the TPO region, a decrease over the North Pacific, and increases over north-eastern North America and Antarctica. The  $\Delta Z_{500}$  response mirrors the  $\Delta Z_{200}$  pattern but with reduced intensity. In contrast, warming in the TIO region induces  $\Delta T_s$  increases over Antarctica and significant warming over the Indian subcontinent, while the Tibetan Plateau experiences cooling. Notably, the northwest of North America shows marked cooling under TIO warming. The  $\Delta Z_{200}$  response to TIO warming displays a dipole pattern, characterized by increases in the tropical warming regions and decreases toward the poles, followed by subsequent increases. The  $\Delta Z_{500}$  response follows a similar trend to  $\Delta Z_{200}$  with weaker intensity. The responses of surface temperature ( $\Delta T_s$ ), meridional wind ( $\Delta V$ ), air temperature ( $\Delta T_a$ ), and humidity ( $\Delta Q$ ) to warmings in these patches are presented in Figure 6, which provide background information to later AHT studies. In response to warmings in the illustrative TPO region, the response of zonal-mean meridional wind is significant in the tropical and subtropical regions, but small at high latitudes. Near the surface around 10°S, as well as at 250 hPa in the upper atmosphere between the equator and 20°S, there is a significant northerly wind anomaly. However, at 100 hPa in the upper atmosphere near 10°S, there is a southerly wind anomaly (Figure

Formatted: Font color: Text 1

Formatted: Font color: Text 1

Formatted: Font color: Text 1

Formatted: Font color: Text 1

Formatted: Font color: Text 1

Formatted: Font color: Text 1

Formatted: Font color: Text 1

Formatted: Font color: Text 1

Formatted: Font color: Text 1

Formatted: Font color: Text 1

Formatted: Font color: Text 1

Formatted: Font color: Text 1

Formatted: Font color: Text 1

Formatted: Font color: Text 1

Formatted: Font color: Text 1

Formatted: Font color: Text 1

Formatted: Font color: Text 1

Formatted: Font color: Text 1

Formatted: Font color: Text 1

Formatted: Font color: Text 1

Formatted: Font color: Text 1

Formatted: Font color: Text 1

Formatted: Font color: Text 1

Formatted: Font color: Text 1

Formatted: Font color: Text 1

Formatted: Font color: Text 1

Formatted: Font color: Text 1

Formatted: Font color: Text 1

Formatted: Font color: Text 1

Formatted: Font color: Text 1

Formatted: Font color: Text 1

Formatted: Font color: Text 1

Formatted: Font color: Text 1

Formatted: Font color: Text 1

Formatted: Font color: Text 1

Formatted: Font color: Text 1

6b). There is a significant increase in  $\Delta Q$  in the northern hemisphere from the surface up to 550 hPa (Figure 6c). In terms of  $\Delta T$ , warming begins at the surface around  $0^\circ$  and extends upwards to 100 hPa, then propagates towards the poles, and there is an air temperature increase in the Arctic regions (Figure 6d). The increase of Arctic air temperature is a result of enhanced AHT to Arctic regions, which leads to a radiative heating to the surface and radiative cooling to the TOA fluxes. In response to warmings in the illustrative TIO region, there are southerly wind anomalies at the surface around  $10^\circ\text{N}$ , while at higher altitudes, northerly wind anomalies prevail (Figure 6f).  $\Delta Q$  increases in the southern hemisphere, but decreases in the northern hemisphere, indicating a decrease of meridional latent heat transport near  $60^\circ\text{N}$ . TIO warming results in a cooling effect in the Arctic, which is induced by the decrease of AHT to the Arctic regions (Figure 6h).

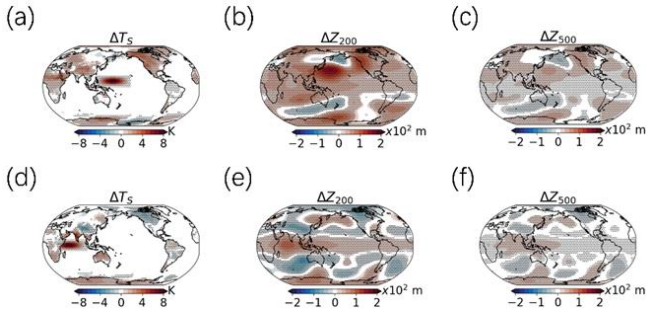


**Figure 8: Spatial distributions of responses in  $\Delta T_s$  (a),  $\Delta Z_{200}$  (b) and  $\Delta Z_{500}$  (c) following increased SST in a patch over the tropical Pacific Ocean (TPO), and in  $\Delta T_s$  (d),  $\Delta Z_{200}$  (e) and  $\Delta Z_{500}$  (f) following increased SST in a patch over the tropical Indian Ocean (TIO). Dotted areas indicate regions that passed the 95% confidence test.**

To quantify the impacts of SST warming over the TPO and TIO on the Arctic AHT, we computed the AHT responses to the warming of the two patches separately. AHT can be calculated as the vertically integrated and zonally averaged transport of moist static energy ( $S$ ). According to Neelin and Held (1987),  $S$  can be defined as follows:

$$S = c_p T_a + LQ + gZ, \quad (59)$$

where  $T_a$  represents atmospheric temperature,  $c_p$  is the specific heat capacity of air at constant pressure,  $L$  denotes the latent heat of vaporization of water,  $Q$  is specific humidity,  $g$  is the acceleration due to gravity, and  $Z$  represents geopotential height. The components of  $S$  will be denoted below by  $S_T$ ,  $S_Q$  and  $S_Z$ , respectively.

425 The poleward transport of moist static energy  $S$  can be decomposed into mean meridional circulation (MOC), stationary eddy (SE), transient eddy (TE), and transient overturning circulation (TOC) components, following the methodologies of Priestley (1948) and Lorenz (1953). According to Donohoe (2020), for each latitude  $\theta$ , atmospheric energy transport is:

$$AHT(\theta) = 2\pi \cos(\theta) \int_0^{P_s} [\bar{V}][\bar{S}] + \overline{[V^*S^*]} + \overline{[V'']S'^*} + \overline{[V']S'} \frac{dp}{g},$$

(610)

430 where  $V$  represents the meridional velocity. Square brackets  $[ ]$  denote zonal averages, overbars  $\overline{(\quad)}$  denote time averages over each month of analysis, asterisks  $(^*)$  are departures from the zonal average, and primes  $(')$  are departures from the time average. The first term signifies the MOC driven by the vertical gradient in  $S$ , taking into account mass conservation in MOC energy transport. The second term is SE, showing poleward transport in warm or moist sectors. These first two terms are derivable from monthly mean data. The third term pertains to the transport associated with TE, primarily baroclinic synoptic eddies. The fourth term involves energy transport by the covariance between zonal-mean overturning circulation and vertical stratification, referred to as TOC, which is significantly smaller than the other components and thus often excluded in AHT discussions.

440 Figure 7-9 shows the changes in AHT and its components in response to warmings in the TPO and TIO. AHT response to warmings in TPO at 60°N is positive, and AHT response to warmings in TIO at 60°N is negative. For both cases, AHT to the Arctic region is dominated by SE (Figure 7b), and the opposite SE response to TPO and TIO leads to opposite responses in AHT, which also causes different responses of TOA and surface energy budgets in the Arctic regions. Additionally, Figures 7-9(c) and (d) further dissect the SE responses to warmings in the TPO and TIO, respectively, and the results indicate that dry static energy predominantly drives the SE response to warmings in both TPO and TIO.

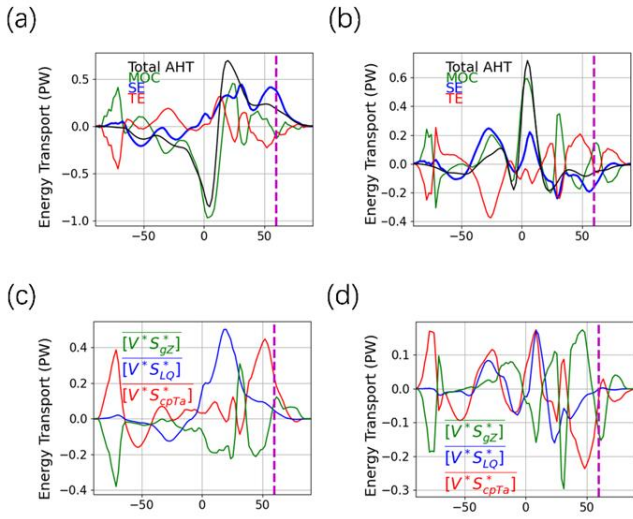


**Figure 79: Decomposition of meridional AHT.** (a) and (b) display show the changes in meridional AHT following SST warming in the TPO and TIO, respectively. The total AHT is represented by a thick black line, while the contributions from the MOC, SE, and TE are depicted by fine lines in green, blue, and red, respectively. Panels (c) and (d) detail the decomposition of the SE component from (a) and (b), with the contributions from Z, Q, and T shown in green, blue, and red, respectively. The purple dotted line represents the 60°N latitude line.

To better understand the opposite response of SE heat flux to warmings in TPO and TIO, we analyzed the spatial distribution of SE heat fluxes. The vertically integrated SE heat flux ( $\phi$ ) can be computed through the following integral. Following the approach outlined by Yohai Kaspi (2013), the calculation of SE heat flux denoted as  $V^*S^*$  involves the direct subtraction of zonal and time mean components:

$$V^*S^* = \overline{VS} - \overline{V}\overline{S} - [\overline{V}][\overline{S}], \quad (7)$$

and the vertically integrated SE heat flux ( $\phi$ ) can be computed through the following integral:

$$\phi = \int_0^{P_s} V^*S^* \frac{dp}{g}, \quad (811)$$

In response to warmings in the TPO, the vertically integrated SE heat flux exhibits significant oscillatory characteristics over the Pacific Ocean. According to Figure 8(a),  $\phi$  increases in the western tropical Pacific, decreases over the north-west and

central Pacific, and then increases again over the northeastern Pacific and Alaska. Over land,  $\phi$  increases over north-east Asia, the Tibetan Plateau and Europe, decreases over north-east Asia, increases over the Tibetan Plateau and Europe. This phenomenon is consistent to Goss et al. (2016), who found that warming in the low-latitude Pacific leads to increased  $\phi$  in higher latitudes.

Combining Eqs. (9) and (71) and Eq. (10), we are able to further attribute  $\phi$  to changes in dry static heat flux ( $\Delta\phi_{Ta}$ ), latent heat flux ( $\Delta\phi_Q$ ), and potential energy ( $\Delta\phi_Z$ ), respectively. Among the three main contributing factors to  $\Delta\phi$ ,  $\Delta\phi_{Ta}$  aligns closely with the overall  $\Delta\phi$  pattern, indicating it as the primary contributor (Figure 8b10b). The spatial pattern of  $\Delta\phi_{Ta}$  can be explained by the change of  $\Delta V^*$  and  $\Delta S_{Ta}^*$  (Figure-Figs 108c-d), which reflects the spatial pattern of stationary waves. In addition,  $\Delta\phi_Q$  is large in the low latitudes, but is small near the poles (Figure. 8e10e). Interestingly, the  $\Delta\phi_Z$  exhibits an opposite pattern to  $\Delta\phi$  in the northern hemisphere (Figure 10f). Despite the fact that the changes in  $\Delta S_Z^*$  have a similar spatial distribution to  $\Delta S_{Ta}^*$  (Figure 10h), the  $\Delta\phi_Z$  shows an opposite trend to  $\Delta\phi_{Ta}$  due to the differing correlation between  $\Delta V^*$  and  $\Delta S_Z^*$ . This indicates that while  $\Delta S_Z^*$  increases in regions where  $\Delta V^*$  also increases, their combined effect on  $\Delta\phi_Z$  leads to a negative contribution compared to  $\Delta\phi$ . The  $\Delta\phi_Z$  pattern is also similar to  $\Delta\phi$  but with lower values (Fig. 8f). The spatial pattern of  $\Delta\phi_Q$  and  $\Delta\phi_Z$  can be understood by the change of  $\Delta V^*$ ,  $\Delta S_Q^*$  and  $\Delta S_Z^*$  (Figures 8e, g, h).

In response to warmings in the TIO, the spatial pattern of  $\Delta\phi$  oscillation is quite different from the TPO case. The transfer of SE heat flux encounters obstacles near the Tibetan Plateau, which might explain why the response of  $\Delta\phi$  is different in the Northern hemisphere and the Southern hemisphere. Globally,  $\Delta\phi_{Ta}$  remains the dominant contributor to  $\Delta\phi$ , while  $\Delta\phi_Q$ 's contribution remains relatively low. Notably, in the Tibetan Plateau region,  $\Delta\phi_Z$  becomes the primary driver of  $\Delta\phi$  (Figures 10i-n).  $\Delta\phi_{Ta}$  remains dominant,  $\Delta\phi_Q$ 's contribution is low, and  $\Delta\phi_Z$  mirrors the  $\Delta\phi$  pattern (Figs. 8i-n).

Based on these results, we are able to understand why the responses of AHT near 60°N to warmings in TPO and TIO are different. TPO warming triggers local northward SE, leading to significant energy fluctuation amplitude in the mid-to-high latitude Pacific, thereby enhancing meridional energy flow northward. This mechanism facilitates the influx of warm, moist air into the Arctic, ultimately causing Arctic warming. Conversely, in the TIO, the Tibetan Plateau effects the poleward propagation of SE in the tropical warm pool, and the SE responses finally leads to Arctic cooling. The response of stationary waves to warmings in these two regions are different, so the poleward moist static energy transported by SE is also different, leading to opposite AHT responses. These findings support the research results of Goss et al. (2016) and the tropical excitation mechanism for Arctic warming outlined by Lee et al. (2011).

We also note that the northeastward SE induced by TPO is stronger than the southeastward SE, while the SE intensity in both directions induced by TIO is similar but significantly weaker than that induced by TPO. This may also contribute to the faster Arctic warming compared to Antarctica in response to tropical SST increases. This could be due to the Antarctic's geographical location and oceanic isolation, which make it less responsive to tropical SST changes. The Southern Ocean, strong westerly winds, and the Antarctic Circumpolar Current act as thermal barriers, limiting heat transport from lower latitudes (Marshall, 2003). In contrast, the Arctic's surrounding land and ocean allow more effective heat transport from

lower to higher latitudes (Serreze et al., 2011). Additionally, differences in atmospheric circulation patterns play a significant role: the circumpolar westerlies in the Southern Hemisphere weaken meridional heat transport, limiting the direct impact of tropical regions (Thompson et al., 2002). In the Northern Hemisphere, the Arctic benefits from teleconnection patterns like the North Atlantic Oscillation and the Arctic Oscillation, which enhance heat transport towards the Arctic (Overland et al., 2010).

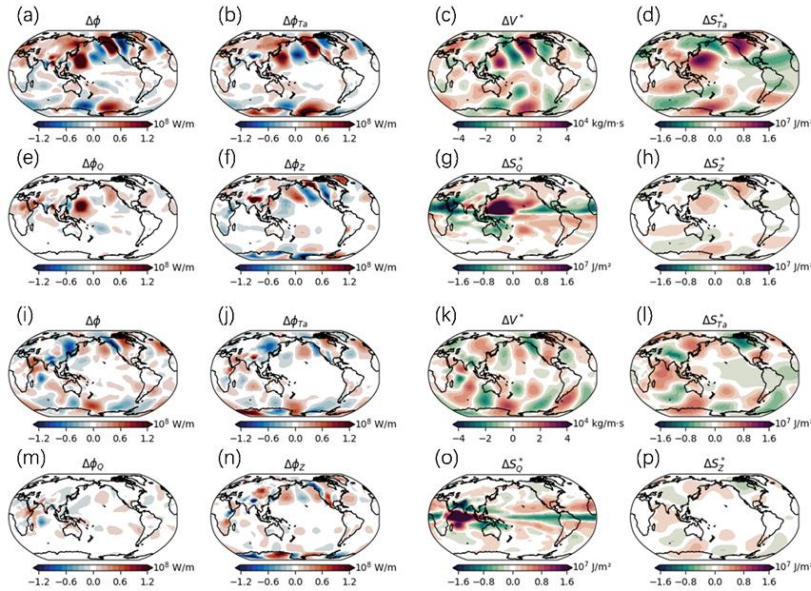


**Figure 810:** (a)  $\Delta\phi$  induced by SST warming in the TPO. (b) The contribution of  $\Delta\phi_{Ta}$  to the SE. (c) The vertical integration of  $\Delta V^*$  from the surface to the TOA. (d) The vertical integration of  $\Delta S_{Ta}^*$  from the surface to the TOA. (e) The contribution of  $\Delta\phi_Q$  to the SE. (f) The contribution of  $\Delta\phi_Z$  to the SE. (g) The vertical integration of  $\Delta S_Q^*$  from the surface to the TOA. (h) The vertical integration of  $\Delta S_Z^*$  from the surface to the TOA. (i-p) are same as (a-h) but for responses to warming in the TIO. (j) Same as (b) but for the TIO. (k) Same as (c) but for the TIO. (l) Same as (d) but for the TIO. (m) Same as (e) but for the TIO. (n) Same as (f) but for the TIO. (o) Same as (g) but for the TIO. (p) Same as (h) but for the TIO.

### 3.3 Reconstruction of polar energy budget based on the Green's function approach

The response of PEB to regional SST changes might be used to qualitatively explain how SST variations affect PEB.

The sensitivity of the PEB to SST perturbations within a specific grid box, identified by index  $i$ , can be estimated using the following equation (Zhou et al. 2017):

$$\left(\frac{\partial R}{\partial SST_i}\right)_p = \frac{\sum_p \Delta SST_p \left(\frac{\partial R}{\partial SST_p}\right)_p}{\sum_p \Delta SST_p} = \frac{\partial R}{\partial SST_p} \frac{S_i}{S_p}, \quad (9)$$

where  $R$  denotes a specific energy flux,  $S_i$  and  $S_p$  represent the ocean surface area of the specific grid point and the patch, respectively, and  $\Delta SST_p$  is the SST anomaly in the  $p$ th patch [Eq. (1), noting that  $\Delta SST_p$  equals zero for grid points outside of a patch], and  $SST_i$  denotes the SST in the  $i$ th grid box.  $\left(\frac{\partial R}{\partial SST_p}\right)_p$  reflects the average response of  $R$  to a 1 K increase in SST

within a specific grid box inside the patch. Additionally,  $\frac{\partial R}{\partial SST_p}$  illustrates the variation in the PEB per unit of patch-averaged SST change, derived from experiments involving conjugate  $\pm 1$  K patch warming. The sensitivity for grid boxes within a single patch corresponds to the average  $R$  change due to a 1 K warming within that specific grid box. For grid boxes overlapping multiple patches, the sensitivity is determined by the weighted average value  $\left(\frac{\partial R}{\partial SST_i}\right)_p$ . The sensitivities of PEB to SST perturbation in each grid box are shown in Figure 9.

Utilizing these sensitivities, we can reconstruct the PEB response to arbitrary changes in SST through the Green's function approach, represented as:

$$\Delta R = \sum_i \frac{\partial R}{\partial SST_i} \Delta SST_i + c_f, \quad (10)$$

where  $c_f$  is an error term, which represents the contributions from nonlinearities and non-SST induced factors.

Then we use the Green's function approach to reconstruct the AHT in response to 8 different SST patterns in the EOF-SST experiments (Figures 10a-h), and the Green's function reconstructed AHT are then compared to model-produced values in the EOF-SST experiments (Figures 10i-j). The results show that the majority of the experimental simulations of  $\Delta R_{\text{aht}}$  align closely with the  $\Delta R_{\text{aht}}$  reconstructed by the Green's function, lying near the  $y = x$  line. The biases of the Green's function reconstructed values are partially induced by the SST change inside the Arctic region, which is not captured by the Green's function reconstruction, and non-linear terms also contribute to the bias. Therefore, the Green's function approach can qualitatively explain how the SST perturbation patterns in Figure 10(a-h) affects PEB.

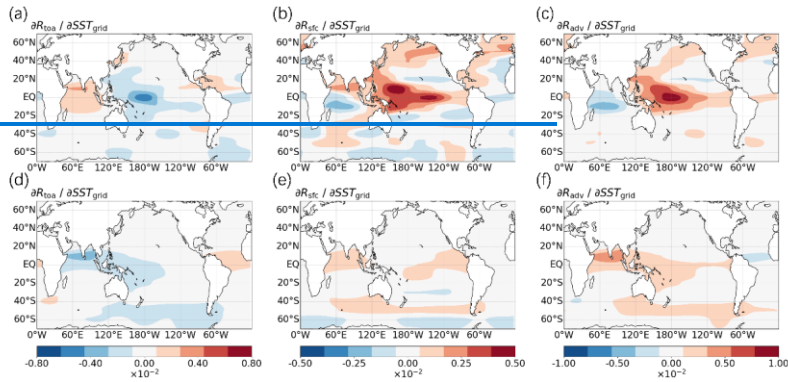


**Figure 9:** The sensitivity of (a)  $\partial R_{toa}/\partial SST_t$  of Arctic, (b)  $\partial R_{sc}/\partial SST_t$  of Arctic, (c)  $\partial R_{adv}/\partial SST_t$  of Arctic, (d)  $\partial R_{toa}/\partial SST_t$  of Arctic, (e)  $\partial R_{sc}/\partial SST_t$  of Arctic, (f)  $\partial R_{adv}/\partial SST_t$  of Antarctica to surface warming in each grid box, calculated using Eq. (9). The units are  $W/m^2/K$ .



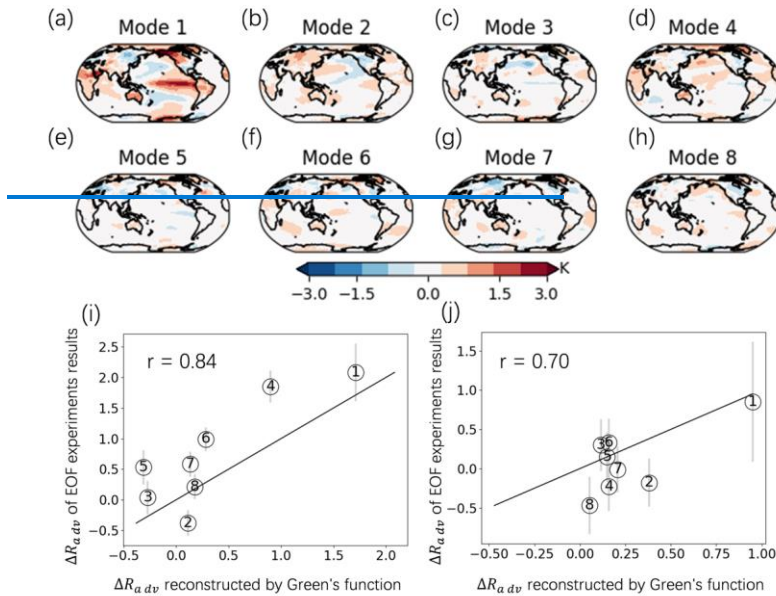


**Figure 10:** (a-h) The surface temperature change patterns in individual EOF-SST experiments. (i) Comparison of Arctic  $\Delta R_{adv}$  responses to different SST change patterns in EOF-SST experiments (y-axis) and that reconstructed by the Green's function approach (x-axis). The digits represent the number of corresponding EOF modes in each experiment. Error bars correspond to the 95 % confidence interval. (j) Response of Antarctica  $\Delta R_{adv}$ .

#### 4 Conclusion

This study delves into the mechanisms behind the responses of radiative budget in high-latitude regions to sea surface warmings in the low latitudes through a series of idealized SST change experiments. It elucidates the mechanisms through which the [PEBpolar energy budget](#) responds to distant SST variations, revealing significant different impacts of SST changes across different oceanic regions on the Arctic and Antarctic energy budgets. These impacts are mediated by alterations in AHT, the distribution of sensible heat flux from stationary eddies, and the interactions among various climatic drivers such as temperature, humidity, and cloud radiative processes.

Specifically, increases in SST in the Pacific and Indian Oceans have [opposing-opposite](#) effects on the Arctic [PEBpolar energy budget](#) in Boreal winter, attributable to different responses of stationary waves to warming in these oceans, which

550 subsequently alter the patterns of poleward AHT. Warming in the Pacific SST tends to enhance heat transport to the Arctic, leading to Arctic air temperature increases, whereas warming in the Indian Ocean ~~diminishes-reduces~~ the heat transport towards the Arctic, resulting in Arctic air temperature decreases. Additionally, the study highlights that the response of the ~~PEB~~polar energy budget varies with the season. During Boreal winter, the sensitivity of the Arctic ~~PEB~~polar energy budget to SST changes in tropical regions is stronger, indicating a higher sensitivity of the polar region to tropical ocean warming in  
555 winter. Using radiative kernels, the contributions of meteorological factors to the TOA radiation response were quantified. The results indicate that ~~changes in -Planck feedback~~air-temperature-change is the primary contributor to changes in polar TOA radiation, while the contributions from clouds and albedo are relatively smaller. The decomposition of surface radiation also shows that ~~the Planck feedback plays a primary role in driving changes in polar surface radiation~~air-temperature-and-surface-temperature-are-the-main-contributors-to-changes-in-polar-surface-radiation. Finally, the study reconstructed the AHT  
560 responses under different EOF-SST modes using the Green's function approach, validating the consistency between the model experiment results and the Green's function reconstructions. Although biases exist in certain EOF modes, partially due to SST changes within the polar regions and non-linear effects, the Green's function method generally provides a reasonable reconstruction of the ~~PEB~~polar energy budget response to SST changes.

The primary findings of the study are summarized as follows:

- 565
1. In response to SST warmings in most tropical and midlatitude regions, polar air temperatures increase due to enhanced AHT, leading to an increase in the polar surface energy budget and a decrease in the polar TOA energy budget.
  2. The response of Arctic AHT to warmings in the tropical Indian Ocean is negative in Boreal winter. Stationary eddies play a crucial role in modulating the polar AHT response to ~~global-tropical~~ SST changes.
  3. Subtropical SST changes have relatively weak impacts on the polar energy budget.

570 The findings of this study have ~~significant~~implications for understanding and predicting polar climate responses to global warming. ~~We find that~~The distinct responses of the Arctic and Antarctic energy budgets to regional SST changes underscore the necessity of considering regional specificity when modeling and predicting climate change. ~~Our findings emphasize the critical role of radiative feedbacks in shaping the polar climate, providing insights that could enhance the accuracy of climate models.~~ The differential impacts of SST changes in various oceanic regions on the polar energy budgets  
575 highlight the importance of incorporating regional specificity in climate models. ~~Aceurate modeling of these impacts is crucial for reliable climate projections.~~ Moreover, the study underscores the ~~pivotal-important~~ role of AHT in modulating polar temperatures, ~~and emphasize the critical role of radiative feedbacks in shaping the polar climate.~~ Understanding the mechanisms of AHT and its interaction with stationary eddies can lead to improved predictions of polar climate responses to global SST changes. The ~~analysis-analyses~~ of radiative feedbacks, including the roles of temperature, humidity, and clouds,  
580 provides a comprehensive understanding of the factors contributing to polar amplification. ~~By focusing on how AHT redistributes heat poleward and influences atmospheric circulation patterns, we gain a comprehensive understanding of the factors contributing to polar amplification. This knowledge can be utilized to refine models of atmospheric heat transport, enhancing their predictive capabilities for polar climate dynamics.~~This knowledge can be utilized to refine radiative transfer

models and enhance their predictive capabilities. Results from only one global climate model are analyzed in this study, and analyses with more climate models might be useful to reduce model biases in future studies.

Author Contributions

Methodology: Chen Zhou;  
Investigation: Qingmin Wang;  
Writing – original draft preparation: Qingmin Wang;  
Writing – review & editing: Chen Zhou, Yincheng Liu, Lujun Zhang.

Code Availability

The code used in this study are available upon request from the corresponding author.

Acknowledgements

This work is supported by NSFC 42375038.

Competing interests

The contact author has declared that none of the authors has any competing interests.

References

Alexeev, V. A., Langen, P. L., and Bates, J. R.: Polar amplification of surface warming on an aquaplanet in “ghost forcing” experiments without sea ice feedbacks, *Clim. Dyn.*, 24, 655–666, <https://doi.org/10.1007/s00382-005-0018-3>, 2005.

Annamalai, H., Okajima, H., and Watanabe, M.: Possible impact of the Indian Ocean SST on the Northern Hemisphere circulation during El Niño, *J. Climate*, 20, 3164–3189, <https://doi.org/10.1175/JCLI4156.1>, 2007.

Armour, K. C., Marshall, J., Scott, J. R., Donohoe, A., and Newsom, E. R.: Southern Ocean warming delayed by circumpolar upwelling and equatorward transport, *Nature Geoscience*, 9, 549–554, <https://doi.org/10.1038/ngeo2731>, 2016.

- Baggett, C. and Lee, S.: An identification of the mechanisms that lead to Arctic warming during planetary-scale and synoptic-scale wave life cycles, *J. Atmos. Sci.*, 74, 1859–1877, <https://doi.org/10.1175/JAS-D-16-0156.1>, 2017.
- 610 Barsugli, J. J. and Sardeshmukh, P. D.: Global atmospheric sensitivity to tropical SST anomalies throughout the Indo-Pacific basin, *J. Clim.*, 15, 3427–3442, [https://doi.org/10.1175/1520-0442\(2002\)015<3427>2.0.CO;2](https://doi.org/10.1175/1520-0442(2002)015<3427>2.0.CO;2), 2002.
- Barton, N. P., Klein, S. A., Boyle, J. S., and Zhang, Y. Y.: Arctic synoptic regimes: Comparing domain-wide Arctic cloud observations with CAM4 and CAM5 during similar dynamics., 117, D15205, <https://doi.org/10.1029/2012JD017589>, 2012.
- Boeke, R. C. and Taylor, P. C.: Seasonal energy exchange in sea ice retreat regions contributes to differences in projected
- 615 Arctic warming, *Nat. Commun.*, 9, 5017, <https://doi.org/10.1038/s41467-018-07061-9>, 2018.
- Budyko, M. I.: The effect of solar radiation variations on the climate of the Earth, *Tellus*, 21, 611–619, <https://doi.org/10.3402/tellusa.v21i5.10109>, 1969.
- Cao, G. and Zhang, G. J.: Role of vertical structure of convective heating in MJO simulation in NCAR CAM5.3, *J. Clim.*, 30, 7423–7439, <https://doi.org/10.1175/JCLI-D-16-0913.1>, 2017.
- 620 Chung, C. E. and Räisänen, P.: Origin of the Arctic warming in climate models, *Geophys. Res. Lett.*, 38, L21704, <https://doi.org/10.1029/2011GL049816>, 2011.
- [Dai, A., Luo, D., Song, M., and Liu, J.: Arctic amplification is caused by sea-ice loss under increasing CO<sub>2</sub>, \*Nat. Commun.\*, 10, 121, <https://doi.org/10.1038/s41467-018-07954-9>, 2019.](#)
- Dickinson, R. E., Meehl, G. A., and Washington, W. M.: Ice-albedo feedback in a CO<sub>2</sub>-doubling simulation, *Climatic Change*,
- 625 10, 241–248, <https://doi.org/10.1007/BF00143904>, 1987.
- [Ding, Q., Wallace, J. M., Battisti, D. S., and Steig, E. J.: Tropical forcing of the recent rapid Arctic warming in northeastern Canada and Greenland, \*Nature\*, 509, 209–212, <https://doi.org/10.1038/nature13260>, 2014.](#)
- Donohoe, A., Armour, K. C., Roe, G. H., Battisti, D. S., and Hahn, L.: The partitioning of meridional heat transport from the last glacial maximum to CO<sub>2</sub> quadrupling in coupled climate models, *J. Clim.*, 33, 4141–4165, [https://doi.org/10.1175/JCLI-](https://doi.org/10.1175/JCLI-D-19-0797.1)
- 630 [D-19-0797.1](#), 2020.
- Duan, L., Cao, L., and Caldeira, K.: Estimating contributions of sea ice and land snow to climate feedback, *J. Geophys. Res. Atmos.*, 124, 199–208, <https://doi.org/10.1029/2018JD029093>, 2019.
- Fletcher, C. G. and Kushner, P. J.: The role of linear interference in the annular mode response to tropical SST forcing, *J. Clim.*, 24, 778–794, <https://doi.org/10.1175/2010JCLI3735.1>, 2011.
- 635 Goss, M., Feldstein, S. B., and Lee, S.: Stationary wave interference and its relation to tropical convection and Arctic warming, *J. Clim.*, 29, 1369–1389, <https://doi.org/10.1175/JCLI-D-15-0267.1>, 2016.
- Graversen, R. G. and Burtu, M.: Arctic amplification enhanced by latent energy transport of atmospheric planetary waves, *Q.J.R. Meteorol. Soc.*, 142, 2046–2054, <https://doi.org/10.1002/qj.2802>, 2016.
- Hahn, L. C., Armour, K. C., Zelinka, M. D., Bitz, C. M., and Donohoe, A.: Contributions to polar amplification in CMIP5 and
- 640 CMIP6 models, *Front. Earth Sci.*, 9, 710036, <https://doi.org/10.3389/feart.2021.710036>, 2021.

Hall, A.: The Role of Surface Albedo Feedback in Climate, *J. Clim.*, 17, 1550–1568, [https://doi.org/10.1175/1520-0442\(2004\)017<1550>2.0.CO;2](https://doi.org/10.1175/1520-0442(2004)017<1550>2.0.CO;2), 2004.

Jeong, H., Park, H.-S., Stuecker, M. F., and Yeh, S.-W.: Distinct impacts of major El Niño events on Arctic temperatures due to differences in eastern tropical Pacific sea surface temperatures, *Sci. Adv.*, 8, eabl8278.

645 Kaspi, Y. and Schneider, T.: The role of stationary eddies in shaping midlatitude storm tracks, *J. Atmos. Sci.*, 70, 2596–2613, <https://doi.org/10.1175/JAS-D-12-082.1>, 2013.

Lañé, A., Yoshimori, M., and Abe-Ouchi, A.: Surface Arctic amplification factors in CMIP5 models: Land and oceanic surfaces and seasonality, *J. Clim.*, 29, 3297–3316, <https://doi.org/10.1175/JCLI-D-15-0497.1>, 2016.

650 Lee, S., Gong, T. T., Johnson, N. C., Feldstein, S. B., and Pollard, D.: On the possible link between tropical convection and the Northern Hemisphere Arctic surface air temperature change between 1958 and 2001, *J. Clim.*, 24, 4350–4367, <https://doi.org/10.1175/2011JCLI4003.1>, 2011.

Lee, S.: Testing of the Tropically Excited Arctic Warming Mechanism (TEAM) with Traditional El Niño and La Niña, *J. Clim.*, 25, 4015–4022, <https://doi.org/10.1175/JCLI-D-12-00055.1>, 2012.

655 Lee, S.: A Theory for Polar Amplification from a General Circulation Perspective, *Asia-pacific J. Atmos. Sci.*, 50, 31–43, <https://doi.org/10.1007/s13143-014-0024-7>, 2014.

Lenssen, N. J. L., Schmidt, G. A., Hansen, J. E., Menne, M. J., Persin, A., Ruedy, R., et al.: Improvements in the GISTEMP uncertainty model, *J. Geophys. Res. Atmos.*, 124, 6307–6326, <https://doi.org/10.1029/2018JD029522>, 2019.

Li, Z.-X. and Le Treut, H.: Cloud-radiation feedbacks in a general circulation model and their dependence on cloud modelling assumptions, *Clim. Dyn.*, 7, 133–139, <https://doi.org/10.1007/BF00211155>, 1992.

660 Li, X., Cai, W., Meehl, G.A. et al. Tropical teleconnection impacts on Antarctic climate changes. *Nat Rev Earth Environ.*, 2, 680–698, <https://doi.org/10.1038/s43017-021-00204-5>, 2021.

Liu, Y., Huang, Y., Yuan, J., Xie, Y., Zhou, C.: Contribution of surface radiative effects, heat fluxes and their interactions to land surface temperature variability, *J. Geophys. Res. Atmos.*, 129, e2023JD039495, <https://doi.org/10.1029/2023JD039495>, 2024.

665 Lorenz, E. N.: Available potential energy and the maintenance of the general circulation, *Tellus*, 7, 157–167, 1955.

Marshall, J., Scott, J. R., Armour, K. C., Campin, J.-M., Kelley, M., and Romanou, A.: The ocean's role in the transient response of climate to abrupt greenhouse gas forcing, *Clim. Dyn.*, 44, 2287–2299, <https://doi.org/10.1007/s00382-014-2308-0>, 2015.

670 Lubin, D., and Vogelmann, A. M.: A climatologically significant aerosol longwave indirect effect in the Arctic, *Nature*, 439, 453–456, <https://doi.org/10.1038/nature04449>, 2006.

Marshall, G. J.: Trends in the Southern Annular Mode from observations and reanalyses, *J. Climate*, 16, 4134–4143, [https://doi.org/10.1175/1520-0442\(2003\)016<4134>2.0.CO;2](https://doi.org/10.1175/1520-0442(2003)016<4134>2.0.CO;2), 2003.

Mitchell, J. F. B., Senior, C. A., and Ingram, W. J.: CO<sub>2</sub> and climate: a missing feedback?, *Nature*, 341, 132–134, <https://doi.org/10.1038/341132a0>, 1989.

Neale, R. B., and Coauthors: Description of the NCAR Community Atmosphere Model (CAM 5.0), <https://doi.org/10.5065/D6N877R0>, 2012.

Neelin, J. D. and Held, I. M.: Modeling tropical convergence based on the moist static energy budget, *Mon. Weather Rev.*, 115, 3–12, [https://doi.org/10.1175/1520-0493\(1987\)115<0003>2.0.CO;2](https://doi.org/10.1175/1520-0493(1987)115<0003>2.0.CO;2), 1987.

North, G. R.: Theory of Energy-Balance Climate Models, *J. Atmos. Sci.*, 32, 2033–2043, 2007.

680 [Overland, J. E., and Wang, M.: Large-scale atmospheric circulation changes are associated with the recent loss of Arctic sea ice, \*Tellus A\*, 62, 1–9, <https://doi.org/10.1111/j.1600-0870.2009.00421.x>, 2010.](#)

Park, H.-S., Kim, S.-J., Seo, K.-H., Stewart, A. L., Kim, S.-Y., and Son, S.-W.: The impact of Arctic sea ice loss on mid-Holocene climate, *Nat. Commun.*, 9, 4571, <https://doi.org/10.1038/s41467-018-07068-2>, 2018.

[Pierrehumbert, R. T.: Principles of Planetary Climate, Cambridge University Press, Cambridge, UK, 2010.](#)

685 [Pithan, F., Medeiros, B., and Mauritsen, T.: Mixed-phase clouds cause climate model biases in Arctic wintertime temperature inversions, \*Clim. Dyn.\*, 43, 289–303, <https://doi.org/10.1007/s00382-013-1964-9>, 2014.](#)

Priestley, C. H. B.: Dynamical control of atmospheric pressure: II—the size of pressure systems, *Q. J. R. Meteorol. Soc.*, 74, 67–72, <https://doi.org/10.1002/qj.49707431908>, 1948.

[Pithan, F., Medeiros, B., and Mauritsen, T.: Mixed-phase clouds cause climate model biases in Arctic wintertime temperature inversions, \*Clim. Dyn.\*, 43, 289–303, <https://doi.org/10.1007/s00382-013-1964-9>, 2014.](#)

690 [Rodgers, K. B.: A tropical mechanism for Northern Hemisphere deglaciation, \*Geochem.Geophys.Geosyst.\*, 4, 1046, <https://doi.org/10.1029/2003gc000508>, 2003.](#)

Salzmann, M.: The polar amplification asymmetry: Role of Antarctic surface height, *Earth Syst. Dynam.*, 8, 323–336, <https://doi.org/10.5194/esd-8-323-2017>, 2017.

695 [Sellers, W. D.: A Global Climatic Model Based on the Energy Balance of the Earth-Atmosphere System, \*J. Appl. Meteorol.\*, 8, 392–400, \[https://doi.org/10.1175/1520-0450\\(1969\\)008<0392>2.0.CO;2\]\(https://doi.org/10.1175/1520-0450\(1969\)008<0392>2.0.CO;2\), 1969.](#)

Sejas, S. A., Cai, M., Hu, A., Meehl, G. A., Washington, W., and Taylor, P. C.: Individual feedback contributions to the seasonality of surface warming, *J. Clim.*, 27, 5653–5669, <https://doi.org/10.1175/JCLI-D-13-00658.1>, 2014.

Sejas, S. A., and Cai, M.: Isolating the Temperature Feedback Loop and its Effects on Surface Temperature, *J. Atmos. Sci.*, 73, 3287–3303, <https://doi.org/10.1175/JAS-D-15-0287.1>, 2016.

700 [Semmler, T., Pithan, F., and Jung, T.: Quantifying two-way influences between the Arctic and mid-latitudes through regionally increased CO2 concentrations in coupled climate simulations, \*Clim. Dyn.\*, 54, 3307–3321, <https://doi.org/10.1007/s00382-020-05171-z>, 2020.](#)

[Serreze, M. C., and Barry, R. G.: Processes and impacts of Arctic amplification: A research synthesis, \*Global Planet. Change\*, 77, 85–96, <https://doi.org/10.1016/j.gloplacha.2011.03.004>, 2011.](#)

705 [Shaw, T. A. and Tan, Z.: Testing latitudinally dependent explanations of the circulation response to increased CO2 using aquaplanet models, \*Geophys. Res. Lett.\*, 45, 9861–9869, <https://doi.org/10.1029/2018GL078974>, 2018.](#)

Shell, K. M., Kiehl, J. T., Shields, C. A.: Using the radiative kernel technique to calculate climate feedbacks in NCAR's Community Atmospheric Model, *J. Climate*, 21, 2269–2282, <https://doi.org/10.1175/2007JCLI2044.1>, 2008.

710 Smith, D. M., Screen, J. A., Deser, C., Cohen, J., Fyfe, J. C., García-Serrano, J., et al.: The Polar Amplification Model Intercomparison Project (PAMIP) contribution to CMIP6: Investigating the causes and consequences of polar amplification, *Geosci. Model Dev.*, 12, 1139–1164, <https://doi.org/10.5194/gmd-12-1139-2019>, 2019.

Solomon, A., Shupe, M. D., Persson, O., Morrison, H., Yamaguchi, T., Caldwell, P. M., et al.: The sensitivity of springtime Arctic mixed-phase stratocumulus clouds to surface-layer and cloud-top inversion-layer moisture sources, *J. Atmos. Sci.*, 71, 574–595, <https://doi.org/10.1175/JAS-D-13-0179.1>, 2014.

715 Stuecker, M. F., Bitz, C. M., Armour, K. C., Proistosescu, C., Kang, S. M., Xie, S.-P., et al.: Polar amplification dominated by local forcing and feedbacks, *Nat. Clim. Change*, 8, 1076–1081, <https://doi.org/10.1038/s41558-018-0339-y>, 2018.

Taylor, P. C., Kato, S., Xu, K. M., and Cai, M.: Covariance between Arctic sea ice and clouds within atmospheric state regimes at the satellite footprint level, *J. Geophys. Res. Atmos.*, 120, 12656–12678, <https://doi.org/10.1002/2015JD023520>, 2015.

720 Thompson, D. W. J., and Solomon, S.: Interpretation of recent Southern Hemisphere climate change, *Science*, 296, 895–899, <https://doi.org/10.1126/science.1069270>, 2002.

Vavrus, S.: The impact of cloud feedbacks on Arctic climate under greenhouse forcing, *J. Climate*, 17, 603–615, [https://doi.org/10.1175/1520-0442\(2004\)017<0603>2.0.CO;2](https://doi.org/10.1175/1520-0442(2004)017<0603>2.0.CO;2), 2004.

725 Wang, M., Peng, Y., Liu, Y., Liu, Y., Xie, X., and Guo, Z.: Understanding cloud droplet spectral dispersion effect using empirical and semi-analytical parameterizations in NCAR CAM5.3, *Earth Space Sci.*, 7, e2020EA001276, <https://doi.org/10.1029/2020EA001276>, 2020.

Vargas Zeppetello, L. R., Donohoe, A., and Battisti, D. S.: Does surface temperature respond to or determine downwelling longwave radiation?, *Geophys. Res. Lett.*, 46, 2781–2789, <https://doi.org/10.1029/2019GL082220>, 2019.

730 Yoshimori, M., Abe-Ouchi, A., and Laîné, A.: The role of atmospheric heat transport and regional feedbacks in the Arctic warming at equilibrium, *Clim. Dyn.*, 49, 3457–3472, <https://doi.org/10.1007/s00382-017-3523-2>, 2017.

Yu, Y., Taylor, P. C., and Cai, M.: Seasonal variations of Arctic low-level clouds and its linkage to sea ice seasonal variations, *J. Geophys. Res. Atmos.*, 124, 12206–12226, <https://doi.org/10.1029/2019JD031014>, 2019.

Zhou, C., Zelinka, M. D., and Klein, S. A.: Analyzing the dependence of global cloud feedback on the spatial pattern of sea surface temperature change with a Green's function approach, *J. Adv. Model. Earth Syst.*, 9, 2174–2189, <https://doi.org/10.1002/2017MS001096>, 2017.

735 Zhou, J., Lu, J., Hu, Y., and Zelinka, M. D.: Responses of the Hadley circulation to regional sea surface temperature changes, *J. Clim.*, 33, 429–441, <https://doi.org/10.1175/JCLI-D-19-0315.1>, 2020.